Available online at www.sciencedirect.com

ScienceDirect

Acta Materialia 68 (2014) 295–309

Acta MATERIALIA

www.elsevier.com/locate/actamat

Atom probe tomography study of ultrahigh nanocrystallization rates in FeSiNbBCu soft magnetic amorphous alloys on rapid annealing

K.G. Pradeep [a,*], G. Herzer [b], P. Choi [a], D. Raabe [a,*]

[a] Max-Planck-Institut für Eisenforschung GmbH, Max-Planck-Str. 1, 40237 Düsseldorf, Germany
[b] Vacuumschmelze GmbH & Co. KG, Grüner Weg 37, 63450 Hanau, Germany

Received 20 November 2013; accepted 19 January 2014

Abstract

Rapid annealing (4–10 s) induced primary crystallization of soft magnetic Fe–Si nanocrystals in a $Fe_{73.5}Si_{15.5}Cu_1Nb_3B_7$ amorphous alloy has been systematically studied by atom probe tomography in comparison with conventional annealing (30–60 min). It was found that the nanostructure obtained after rapid annealing is basically the same, irrespective of the different time scales of annealing. This underlines the crucial role of Cu during structure formation. Accordingly, the clustering of Cu atoms starts at least 50 °C below the onset temperature of primary crystallization. As a consequence, coarsening of Cu atomic clusters also starts prior to crystallization, resulting in a reduction of available nucleation sites during Fe–Si nanocrystallization. Furthermore, the experimental results explicitly show that these Cu clusters initially induce a local enrichment of Fe and Si in the amorphous matrix. These local chemical heterogeneities are proposed to be the actual nuclei for subsequent nanocrystallization. Nevertheless, rapid annealing in comparison with conventional annealing results in the formation of ~30% smaller Fe–Si nanocrystals, but of identical structure, volume fraction and chemical composition, indicating the limited influence of thermal treatment on nanocrystallization, owing to the effect of Cu.

Keywords: Soft magnets; Nanocrystalline microstructure; Crystallization; Atom probe tomography; Coarsening

1. Introduction

Nanocrystalline FeSiNbBCu alloys obtained after partial devitrification of initially amorphous samples exhibit excellent soft magnetic properties [1–11]. They were first introduced by Yoshizawa et al. [1–3] and are characterized by nano-sized, randomly oriented Fe–Si crystallites embedded in a retained amorphous matrix [6]. The grain size D of an $Fe_{73.5}Si_{15.5}Cu_1Nb_3B_7$ alloy with optimal magnetic properties is only ~10–15 nm [5–12]. Thus, the structural correlation length is much smaller than the domain wall width, resulting in a negligibly small average magneto-crystalline anisotropy [6–8]. This is a pre-condition for low-loss soft magnetic materials [8]. As a result, typical coercivity values of these materials are <1 A m^{-1} [1,11,13].

The desired nanocrystalline state is obtained after partial devitrification of the amorphous state by annealing close to the final stages of primary crystallization. The combined addition of Cu and Nb proved to be the key for obtaining the fine-grained structure [4,6,12]. More importantly, the addition of Cu is decisive, as it introduces chemical inhomogeneity by forming clusters of Cu atoms, thereby providing a high density of nucleation sites for primary crystallization of body-centerd cubic Fe_3Si [12]. Atom probe tomography (APT) studies by Hono et al. [12,14,15] revealed that the Cu clusters that initially formed in the amorphous matrix act as nucleation sites for Fe-rich nanocrystals. For example, fine Cu clusters 5 nm in

* Corresponding author.
E-mail addresses: pradeep@mpie.de (K.G. Pradeep), d.raabe@mpie.de (D. Raabe).

http://dx.doi.org/10.1016/j.actamat.2014.01.031
1359-6454/

diameter were observed to develop on annealing for 10 min at 550 °C [12]. Small-angle neutron scattering (SANS) investigations by Ohnuma et al. [16] further confirmed that the clustering of Cu atoms occurs prior to the crystallization of α-Fe nanocrystals, with the number density of Cu clusters being highest at the crystallization onset stage, for an alloy containing optimum Cu content of e.g. ~1 at.% in the case of an $Fe_{74.5}Si_{13.5}Nb_3B_9$ alloy. Therefore, Cu-addition plays a decisive role in obtaining the finest possible nanocrystalline microstructures and, in turn, the maximum magnetic permeability.

Conventional heat treatments of such alloys to induce Fe_3Si nanocrystallization are carried out for ~0.5–1 h at temperatures between 500 and 600 °C [1–7]. Previous reports indicated that the primary crystallization onset temperature T_{onset} is shifted on rapid annealing (RA; heating rates of 50–200 K s^{-1} by DC Joule heating) to higher temperatures by almost 80–100 °C relative to the T_{onset} of typical conventional annealing (CA) [17]. More recently, it was shown that comparable microstructure and magnetic properties can also be achieved by RA, mainly when ramping up to temperatures of ~600–700 °C for a few seconds [13]. However, the effect of RA on the nucleation and growth kinetics of Fe–Si nanocrystals is largely unknown. Therefore, the objective of this work is twofold: (a) the systematic investigation of the effect of RA (~100–200 K s^{-1}) on the formation of Cu clusters and the associated nucleation mechanisms of Fe–Si nanocrystals; and (b) a comparative microstructure evaluation of the alloy annealed under both rapid and conventional conditions.

2. Experimental procedure

Amorphous $Fe_{73.5}Si_{15.5}Cu_1Nb_3B_7$ (VITROPERM® 800 (reg. trademark of Vacuumschmelze GmbH & Co. KG) ribbons with a thickness of ~20 μm were prepared by rapid solidification from the melt. Partial crystallization of the ribbons was accomplished by RA and by CA. RA was performed in two very different ways: namely, static (RA_1) and continuous (RA_2). RA_1 was performed by introducing the as-prepared amorphous ribbons between two highly conductive Cu blocks pre-heated in the furnace for 15 min at the set temperature while in good contact with each other. The annealing temperature was measured by a thermocouple in close proximity to the Cu blocks. Such a setup facilitates stress-free RA up to the desired temperatures and for a minimum holding time of 10 s. Multiple annealing trials were performed to ensure reproducibility. Alternatively, RA_2 was performed by continuously transporting the ribbons through a furnace with a 10 cm long homogeneous temperature zone (in nitrogen atmosphere) under a small tensile stress of ~50 MPa [13]. RA_2 was also performed at different temperatures, similarly to RA_1 in order to understand the sequence of nanocrystallization. The detailed soft magnetic properties of these samples are

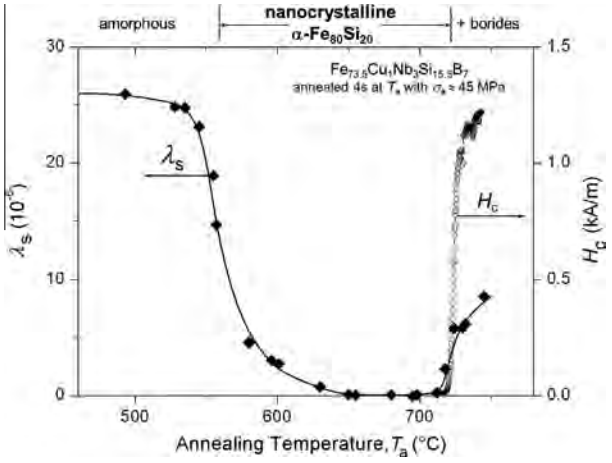

Fig. 1. Variation in saturation magnetostriction λ_s and coercivity H_c as a function of annealing temperature, indicating the various stages from as prepared amorphous to primary Fe–Si nanocrystallization to secondary Fe–B compound formation. Data adapted from Ref. [13].

reported elsewhere [13], but the relevant results for the selected annealing conditions of RA_2 are summarized in Fig. 1. The initial reduction of saturation magnetostriction λ_s at ~550 °C indicates the onset of primary crystallization. Annealing at higher temperatures leads to the continuous reduction of λ_s until it reaches zero at ~650 °C, indicating an increase in crystalline volume fraction with increasing annealing temperature. The onset of secondary crystallization is noticed at ~720 °C, where coercivity, H_c and λ_s tend to increase [13]. Therefore, the annealing window for obtaining optimum nanocrystalline microstructure during primary crystallization by RA is higher by ~100 °C than during conventional differential scanning calorimetric-type slow heating at a rate of ~10 K min^{-1} for prolonged periods of 1 h [11].

Additionally, comparative analysis between RA and CA was performed on those samples annealed close to the initial stages of primary crystallization (with ~30 vol.% crystalline fraction) and at the final stages of primary crystallization (~80 vol.% crystalline fraction). The annealing conditions for preparing such samples are as follows.

1. Initial stages of crystallization: (a) CA_1, 30 min at 480 °C; CA_2, 5 min at 490 °C; and (b) RA_1, 10 s at 555 °C; RA_2, 4 s at 555 °C.
2. Final stage of crystallization: (a) CA_1, 30 min at 575 °C; CA_2, 5 min at 655 °C; and (b) RA_1, 10 s at 695 °C; RA_2, 4 s at 695 °C.

It must be noted that CA_1 and CA_2 were performed in the same furnace as RA_1, but without the use of Cu blocks.

Phase identification and crystallite size measurements were performed using X-ray diffraction (XRD) (General Electric XRD) and transmission electron microscopy (TEM) (Philips CM20 operated at 200 kV). Crystallite sizes

were estimated from XRD peak broadening using the Scherrer equation [18] and also from TEM bright-field (BF) images. The contributions of the amorphous and crystalline phases to the XRD peaks were deconvoluted using a pseudo-Voigt peak profile fitting function. The volume fraction of the crystalline phase was obtained from the ratio of the integral intensity of the crystalline contribution to the total intensity [19]. Thin foil samples for TEM analyses were prepared by electro-polishing using 5% perchloric acid in ethanol at −30 °C and 15 V. The elemental distribution was investigated by APT, which enables three-dimensional (3-D) elemental mapping with near-atomic resolution and high detection sensitivity [20–27]. Therefore, APT enables detailed analyses of size, distribution and chemical composition of nanoscale clusters and crystals [25]. APT experiments were performed with a local electrode atom probe (LEAP™ 3000X HR, Cameca Instruments), applying a voltage pulse fraction (V_p/V_{dc}) of 0.15 at a repetition rate of 200 kHz. The tip temperature was maintained at ~60 K. APT samples were prepared using a dual beam focused ion beam (FEI Helios Nanolab 600) and following the procedures described in Ref. [28]. To minimize beam damage, a low-energy (5 keV) Ga beam was used in the final ion-milling stage. The APT data were evaluated using IVAS 3.6 software provided by Cameca Instruments. Composition profiles with respect to distance from the Cu cluster/amorphous/Fe–Si nanocrystal heterophase interfaces were obtained using the proximity histogram method. An isoconcentration surface of 3 at.% Cu was used as a reference surface for the proxigram analysis, which provided a topologically stable representation of Cu clusters when varying the isoconcentration value ~3 at.% Cu. Unless otherwise mentioned, the use of the isoconcentration surface in depicting Cu clusters is only for clarity and not for quantification. The size and number density of Cu clusters were determined employing the maximum-separation method [29], based on clusters with more than 10 Cu atoms separated by a maximum distance of not more than 0.4 nm [25].

3. Results

3.1. Rapid annealing

3.1.1. XRD

The XRD results of as melt-spun ribbon specimens annealed at various temperature intervals of RA_2 corresponding to the magnetic properties of Fig. 1 are shown in Fig. 2a. The XRD pattern of the as melt-spun sample shows a broad halo peak indicating the presence of a completely amorphous phase, which was also confirmed from the characteristic halo ring pattern (not shown here) in TEM. Annealing even to 535 °C showed no indications of crystallization. On annealing at 555 °C for 4 s, the onset of primary crystallization is realized by the emergence of {220} peak at 53°. This observation is very much in correlation with the reduction in λ_s due to crystallization onset, as shown in Fig. 1. The estimated crystalline volume fraction after peak deconvolution was ~30 vol.%, with a mean crystallite size of 7 nm. Further annealing at higher temperatures resulted in an increase in both the volume fraction and size of DO_3 structured Fe-rich nanocrystals, as summarized in Fig. 2b. The maximum crystalline fraction achieved was 80 vol.%, with an average crystallite size of 10 nm. On annealing at 745 °C, additional diffraction peaks emerged, which corresponds to the crystallization of residual amorphous matrix into Fe–B compounds.

3.1.2. APT

In order to understand the nucleation mechanism of α-Fe nanocrystals during RA_2, APT measurements were performed on the same samples used for XRD analysis. Fig. 3 displays the various stages during nucleation and progressive growth of Cu clusters as a function of annealing temperatures. The as melt-spun amorphous sample showed a homogeneous distribution of all the elements, which has been shown in Fig. 3 for Cu. Binomial frequency distribution analysis (not shown here) also revealed a random distribution of all the elements in the analysed

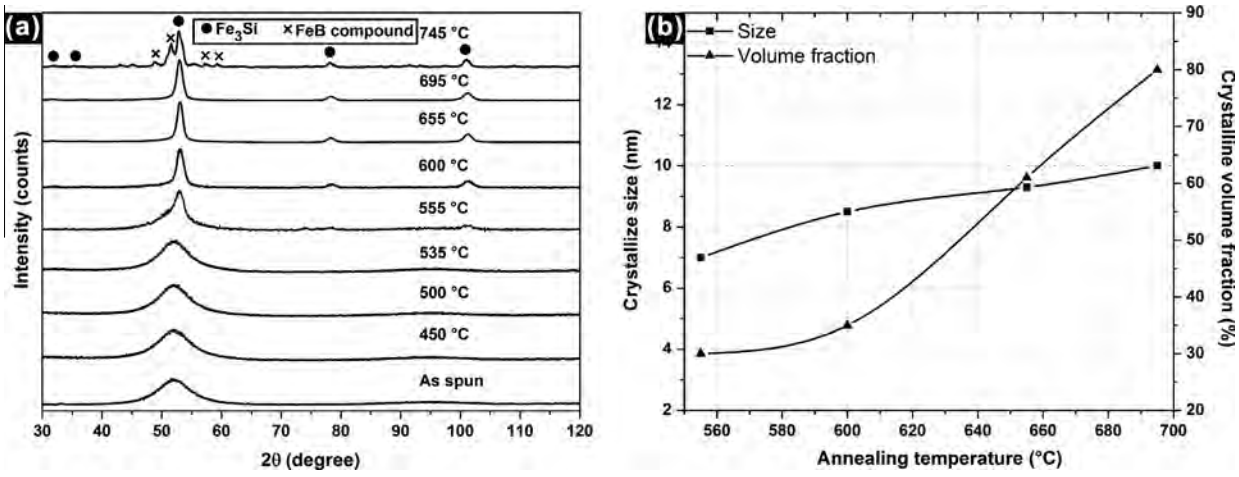

Fig. 2. (a) XRD patterns of a set of rapid annealed samples for a processing duration of 4 s; (b) estimated crystallite size and crystalline volume fraction as a function of annealing temperature.

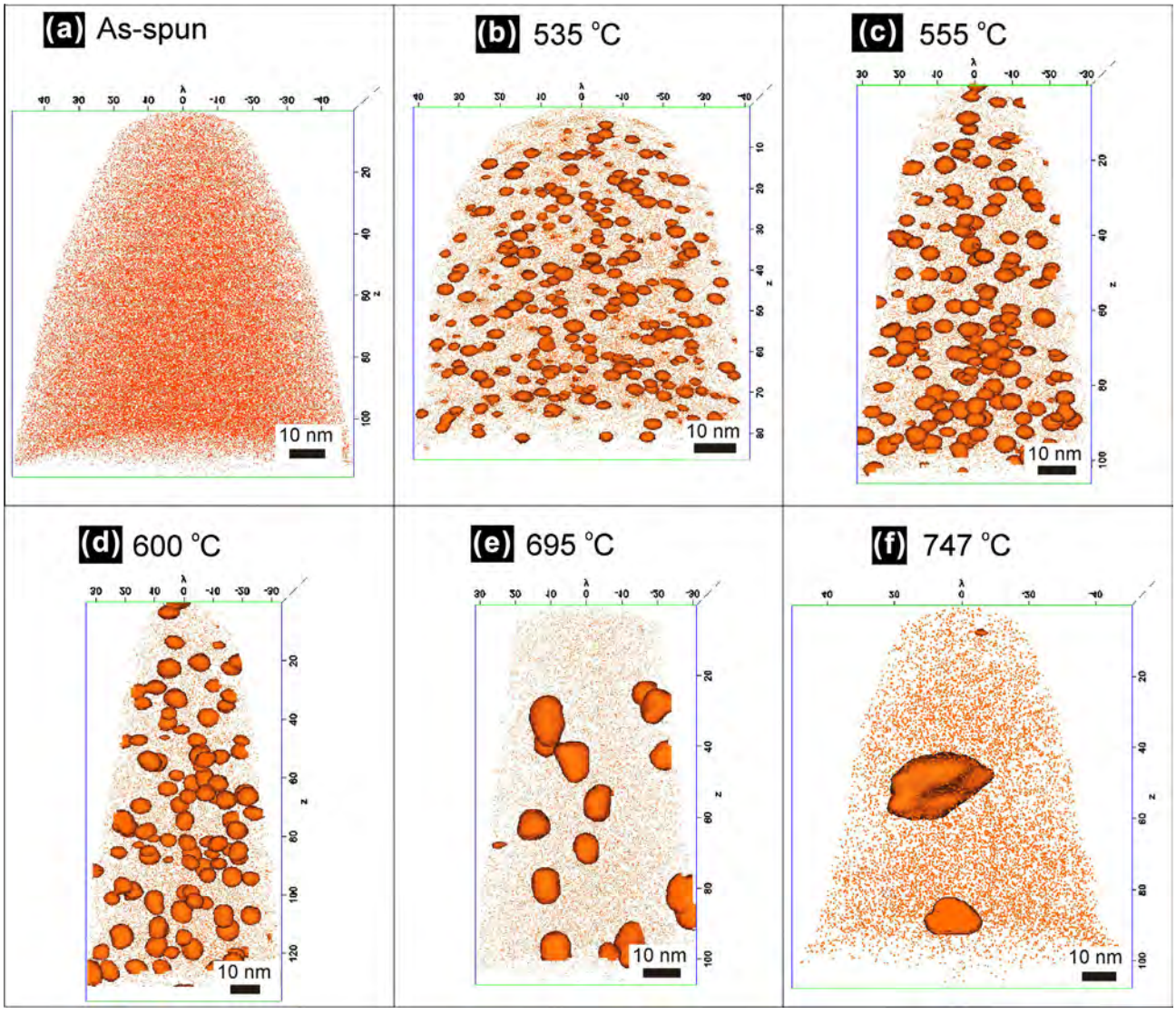

Fig. 3. APT elemental map of Cu (●) and Cu-rich clusters delineated by 3 at.% isoconcentration surfaces when the as-prepared amorphous alloy is rapid annealed for 4 s over a range of annealing temperatures: (a) as-prepared amorphous; (b) 535 °C; (c) 555 °C; (d) 600 °C; (e) 695 °C; (f) 747 °C.

volume. The initial trace of Cu clustering was observed at 450 °C, but could not be defined based on the consideration of a minimum number of Cu atoms ($N_{min} = 10$) to be present for the identification of clusters. At higher annealing temperatures, the Cu clusters are clearly distinguished from the matrix Cu atoms and are visualized in terms of isoconcentration surfaces (for clarity) with a threshold value of 3 at.% Cu in Fig. 3. The size and number density of Cu clusters as a function of annealing temperature are shown in Fig. 4. It must be noted that the clustering of Cu atoms started well before the onset of primary crystallization (555 °C in the case of RA_2) and that the number density of Cu clusters reaches a maximum at 535 °C. Towards the onset of primary crystallization, the number density starts decreasing, indicating the onset of simultaneous coarsening and growth of clusters. It can be noticed in Fig. 4 that, with increasing annealing temperatures, the mean size of the clusters has also increased from

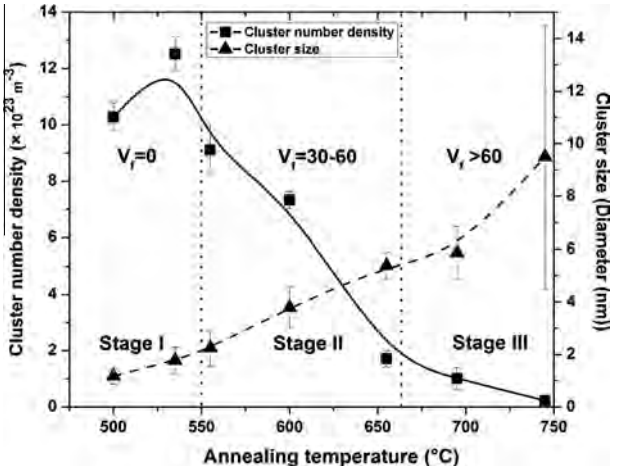

Fig. 4. Variation in Cu cluster number density and size as a function of annealing temperature for 4 s RA.

an initial 1 nm to 9.5 nm at 745 °C, accompanied by a simultaneous reduction in number density. In order to better understand the relation between nucleation of clusters, coarsening and growth with the primary crystallization of DO_3 structured nanocrystals, the sequence of Cu clustering and growth in Fig. 3 is divided into three stages, as indicated in Fig. 4. Stage I corresponds to the onset of Cu clustering prior to primary crystallization. Stage II corresponds to the intermediate temperature range between the onset of primary crystallization with ~30 vol.% crystalline fraction and 60 vol.% crystalline fraction region. Stage III corresponds to the rest of the high temperature annealing range beyond 60 vol.% crystalline fraction.

When interpreting the morphology of clusters in Fig. 3, account has to be taken of the local magnification effect, owing to the fact that Cu has a lower evaporation field (30 V nm^{-1}) than Fe (33 V nm^{-1}) [20]. As a consequence, the Cu clusters are slightly recessed during field evaporation and are therefore projected at a lower magnification towards the detector compared with the matrix atoms. This results in a relatively higher atomic density at the clusters than in the matrix in the 3-D reconstruction [30]. The slightly elongated morphology observed in Fig. 3 for some of the clusters also results from this effect [20,21]. Therefore, to overcome the apparent distortions induced in the clusters as a result of local magnification effects and to determine the average cluster diameter free of distortions, the number of atoms in each cluster identified from the maximum-separation method of the cluster analysis is used to estimate the size, as described in Ref. [25].

3.2. Comparative analysis

3.2.1. Stage I: before primary crystallization

As described earlier and from Fig. 3, on RA_2, Cu clusters form well before the onset of primary crystallization. The initial stages of Cu clustering were noticed on the samples annealed at temperatures significantly lower by at least 50–80 °C (Fig. 4) than those required for primary crystallization (555 °C in this case). Such an inference is in good

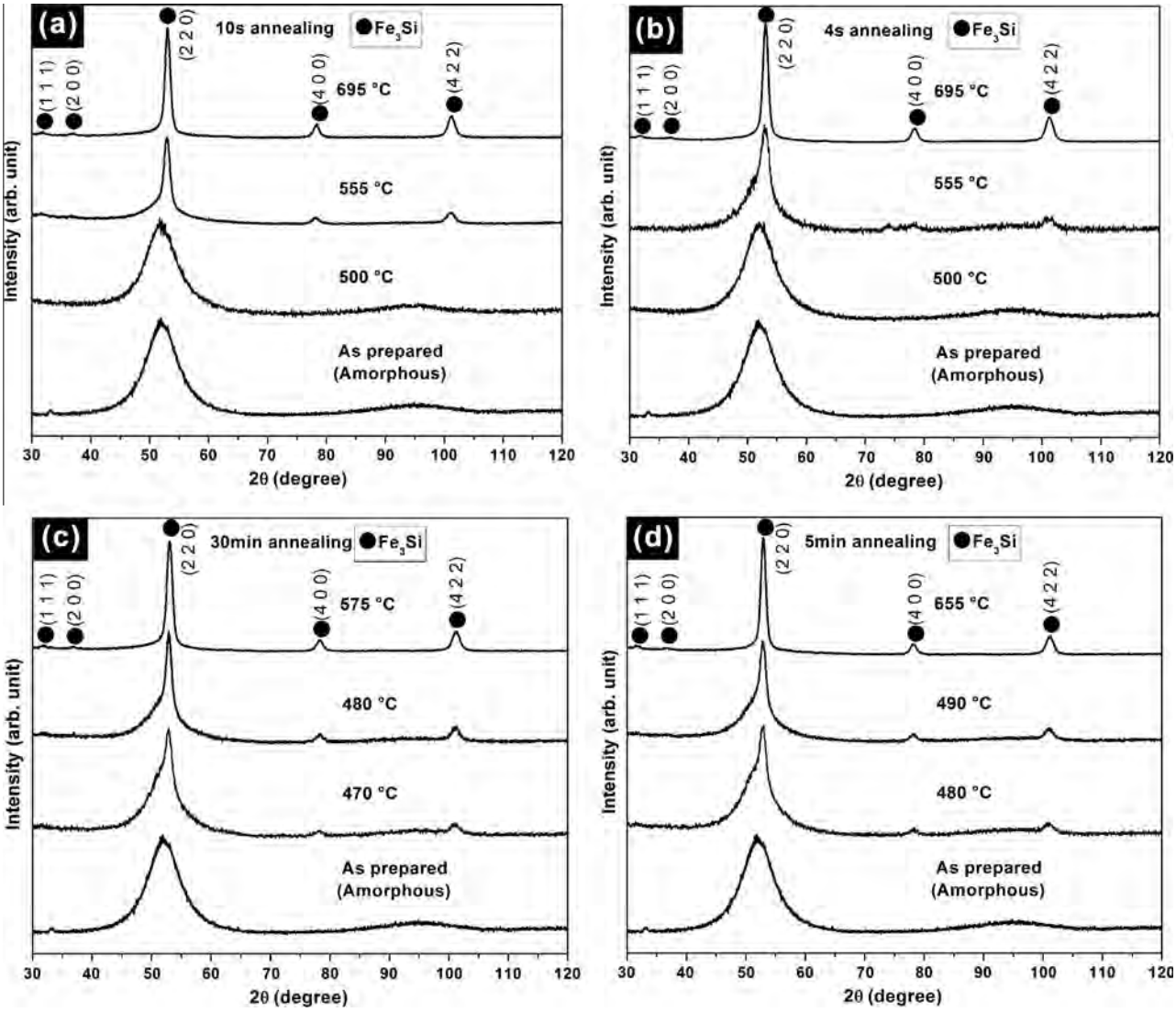

Fig. 5. XRD patterns of a series of RA samples: (a) RA_1: 10 s; (b) RA_2, 4 s; and CA samples: (c) CA_1, 30 min; (d) CA_2, 5 min.

agreement with the previous reports on the onset of Cu clustering prior to primary crystallization on CA [13,14,16,27]. However, a direct comparison between the previously reported CA and the RA investigated in the present work is not feasible, owing to the fact that the onset of clustering is determined by the incubation time at a given temperature. During RA, there is no defined or fixed incubation time, as the overall annealing duration is only 4–10 s, irrespective of the temperature range defined. In contrast, a direct comparison between CA and RA is feasible for primary crystallization events, while taking into account the emerging crystalline volume fraction as a constant parameter over varying annealing time or temperatures.

3.2.2. Stage II: initial crystallization

A shown in Fig. 2a, a series of annealing treatments were performed for RA_1 (10 s holding time) until the onset of primary crystallization was observed at 555 °C (Fig. 5a). The estimated crystalline fraction at this state was ~30 vol.%. Fig. 5b shows the selected XRD plots of RA_2 from Fig. 2, equivalent to the conditions of RA_1. Even though the two methods are very different in terms of annealing procedure and the slightly varying annealing time, the observed results obtained for the onset of crystallization and volume fraction are exactly the same. For comparison, the CA_1 and CA_2 experiments were performed at 480 °C for 30 min and 490 °C for 5 min, as mentioned above, where an equivalent crystalline fraction was obtained (Fig. 5c and d). The TEM characterization of the annealed samples was carried out using BF and selected area electron diffraction (SAED) imaging. Fig. 6a shows the microstructure of the material after CA_2 (5 min at 490 °C). Individual Fe_3Si nanocrystals are separated by envelopes of the amorphous matrix, which are only a few nanometres thick. The amorphous component is hardly detectable in the SAED patterns (Fig. 6b), but BF TEM images taken at different tilt angles clearly show that the Fe_3Si nanocrystals are separated from each other by regions of homogeneous contrast and, therefore, can be identified as the residual amorphous matrix. The inset of Fig. 6a shows the grain size distribution. It can be fitted

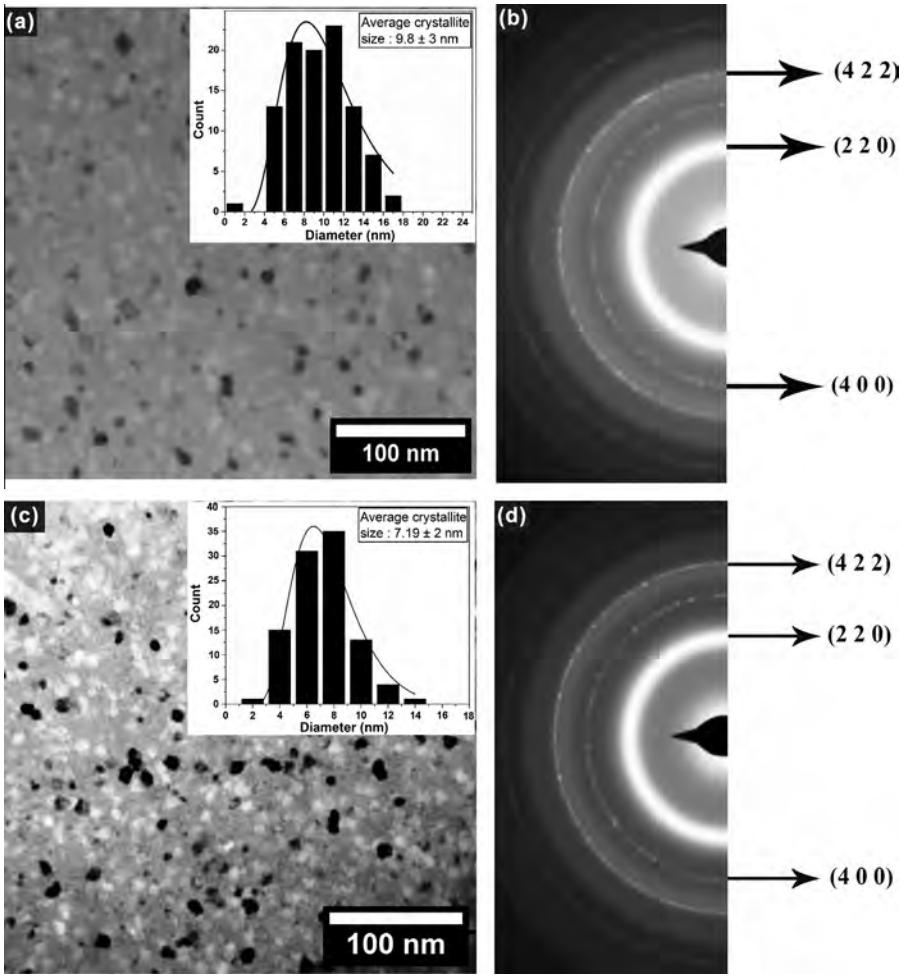

Fig. 6. (a) TEM BF image of 490 °C 5 min conventionally annealed (CA_2) sample with the inset histogram displaying the average crystallite size, (b) corresponding SAED pattern with a typical nanocrystalline ring structure (showing rings of DO_3 structured Fe_3Si nanocrystals), (c) TEM BF image of rapidly annealed sample (RA_2, 4 s at 555 °C) showing randomly oriented nanocrystals with the inset histogram displaying the average crystallite size, and (d) the corresponding SAED pattern.

by a log-normal function with an average crystallite size of 10 ± 3 nm. The nanostructure of the material after RA_2 (4 s at 555 °C) is shown in Fig. 6c. Similar to the sample obtained after CA_2 (in Fig. 6a), Fe_3Si nanocrystals are also separated from each other by thin envelopes of the amorphous matrix. The SAED ring pattern in Fig. 6d confirms the presence of DO_3 structured Fe_3Si nanocrystals similar to CA_2 (see Fig. 6b). The average crystallite size (7 ± 2 nm) of the Fe_3Si phase was determined from a series of BF images and is displayed in the histogram (inset of Fig. 6c). The crystallite sizes estimated from XRD (e.g. for Fig. 2b for RA_2) are in good agreement with those obtained by TEM. The crystallite sizes measured by TEM for all four annealing conditions at the onset of crystallization including RA_1 and CA_1 (the images of which are not shown here) are summarized in Fig. 9a. It was observed that RA (including both cases, RA_1 and RA_2) results in the formation of 30% smaller Fe_3Si nanocrystals than CA (including both cases, CA_1 and CA_2).

3-D elemental maps of the CA_1 (30 min at 480 °C), CA_2 (5 min at 490 °C), RA_1 (10 s at 555 °C) and RA_2 (4 s at 555 °C) samples are shown in Fig. 7a–d. For clarity, only Cu atoms with Cu clusters marked by isoconcentration surfaces are shown in Fig. 7e–h from a defined cylindrical subvolume of $32 \times 32 \times 54$ nm^3 corresponding to Fig. 7a–d. Clusters of varying size ranges are visible. In the case of

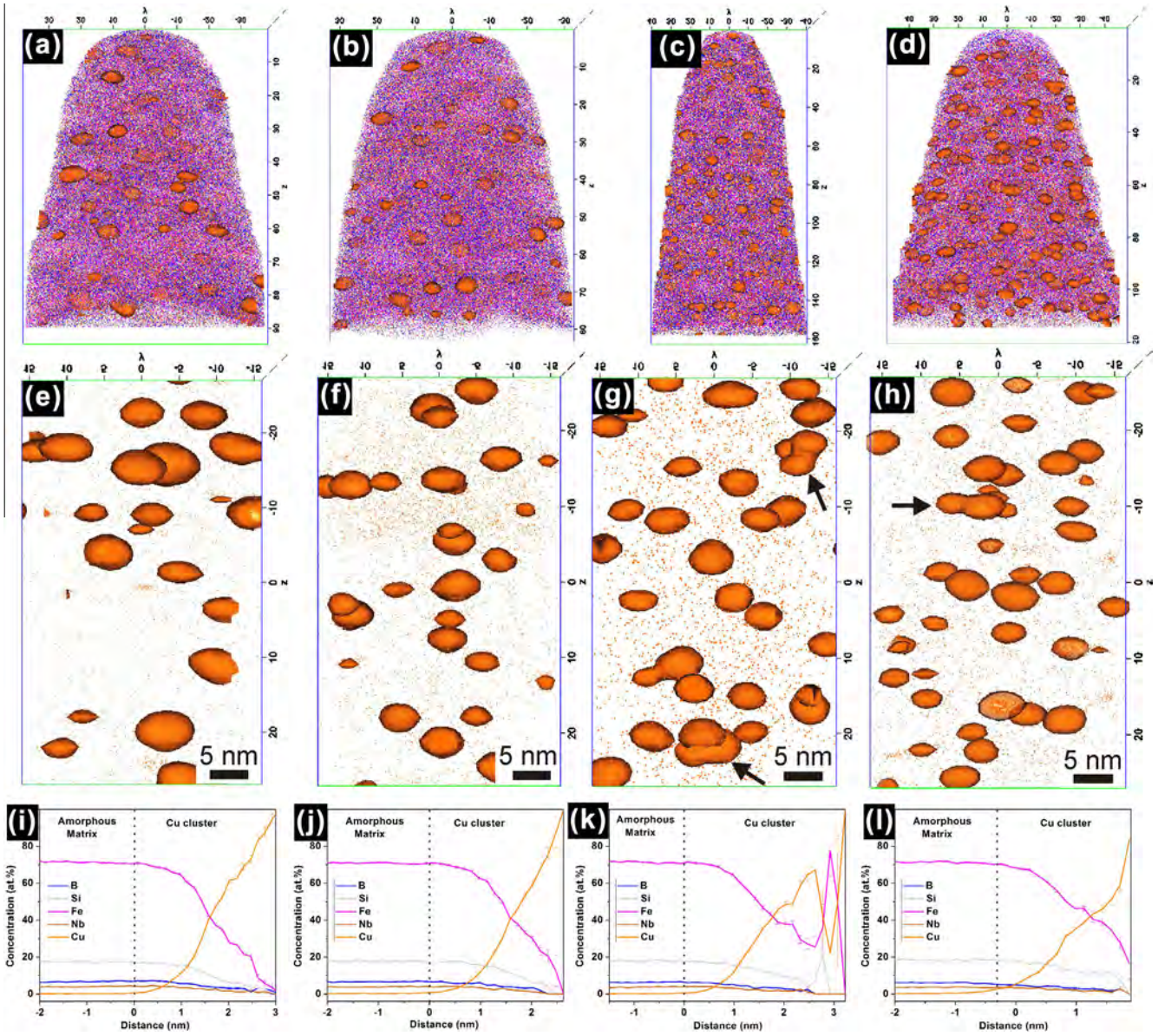

Fig. 7. APT elemental maps of Fe (●), Si (●), Nb (●), B (●), Cu (●) for: (a) CA_1, 480 °C 30 min; (b) CA_2, 490 °C 5 min; (c) RA_1, 555 °C 10 s; (d) RA_2, 555 °C 4 s. Cu atoms with isoconcentration surfaces (3 at.% Cu interface) showing Cu-rich clusters in a representative volume of $32 \times 32 \times 54$ nm^3 for: (e) CA_1, 480 °C 30 min; (f) CA_2, 490 °C 5 min; (g) RA_1, 555 °C 10 s; (h) RA_2, 555 °C 4 s. Coarsening of Cu clusters by interconnected necks are indicated by arrows in (g) and (h). (i), (j), (k), (l) Proximity histogram of 0.15 nm bin size with respect to all the Cu clusters in the analysed volume of (a), (b), (c), (d) for CA and RA samples, respectively.

CA (both CA_1 and CA_2), the average size of the Cu clusters was 3 ± 1 nm diameter, while for RA (both RA_1 and RA_2), the average size was $\sim 2.5 \pm 0.5$ nm (as shown in Fig. 9b). For the calculation of sizes, only those clusters that are fully contained in the reconstructed volume are considered, as some of the clusters near the periphery of the APT tip are sheared. Interestingly, in the elemental maps of RA (both RA_1 and RA_2), instances of Cu clusters being in direct contact with neighbouring clusters are visible, as indicated by arrows in Fig. 7g and h. In order to statistically determine the average concentration values of Cu clusters, proximity histograms of all the clusters in the reconstructed volume in Fig. 7a–d were calculated and are shown in Fig. 7i–l. The proxigram method was used here in order to eliminate the effect of the elongated shapes of the Cu clusters arising from local magnification effects as well as complexities in the morphology of clusters that are in direct contact with each other, as it measures concentrations at fixed distances from an isoconcentration surface, irrespective of the cluster size and shape. The Cu concentrations in the core of all the weighted Cu clusters were found to be $\geqslant 95$ at.% for all RA and CA conditions. It was previously reported that, on annealing, Fe atoms and other solutes are rejected from the Cu-rich regions during cluster formation, which is also confirmed in the present authors' studies [5]. The above-mentioned Cu concentration correlates well with those obtained from a single random Cu cluster (not shown here). However, a difference in the slope of the Cu concentration profile on the right-hand side of the proxigram in Fig. 7k and l of RA is noticed in comparison with the steady increase observed for CA. In fact, a sharp decrease in Cu concentration followed by an immediate increase was noticed in the Cu cluster core region of the proxigram corresponding to RA_1 (Fig. 7k). Enrichment by a factor of 50 with respect to the matrix Cu concentration of 0.4 at.% is observed in the sharp concentration reduction region. Such behaviour further validates the instances of certain Cu clusters being in direct contact with each other, as indicated previously. The number density of Cu clusters estimated from both CA and RA are summarized in Fig. 9d. An estimated $\sim$50–80% increase in the number density of Cu clusters was obtained on RA compared with CA (data calculated from Fig. 7a–d). The slight reduction in number density observed in the case of RA_1 could be mainly due to the increased occurrence of sites where two Cu clusters are in direct contact with each other, as the effect is more pronounced in Fig. 7k compared with Fig. 7l of RA_2. Similar situations are also observed in the case of RA_2, but less frequent in comparison with RA_1. In spite of such anomalies, these findings indicate a substantial increase (up to 80%) in the density of Cu clusters on RA, even though the values of RA are slightly underestimated. Previous reports have shown in great detail the effective role played by Cu atoms in the form of clusters while acting as heterogeneous nucleation sites for Fe_3Si nanocrystallization [12,16,27,31]. Therefore, even a slight increase in the number density of Cu clusters is expected to have a significant effect in the nucleation mechanism of Fe_3Si nanocrystals.

In order to further understand the role of Cu clusters as effective nucleation sites during RA, the number density N of Fe_3Si nanocrystals was calculated from the values of the probed crystal size $D_{Fe\text{–}Si}$ (assuming spherical crystals from Fig. 9a) and the known volume fraction V ($\sim$30 vol.% at the onset of crystallization) as

$$N = \frac{6V}{\pi D^3_{(Fe\text{–}Si)}} \tag{1}$$

The results summarized in Fig. 9c indicate an increase of at least 60–80% for N on RA compared with CA. The values obtained for CA_1 are in good agreement with those reported by Mattern et al. [32]. One can also interpret from Fig. 9d that almost every Cu cluster induces a minimum of one Fe_3Si nanocrystal at the initial stages of crystallization. Therefore, it is concluded that the observed $\sim$80% increase in the number density of Cu clusters on RA has resulted in an identical increase ($\sim$80%) in the number density of Fe_3Si nanocrystals compared with CA. Therefore, by employing RA, extremely high rates for heterogeneous nucleation are achieved, resulting in massive primary crystallization of soft magnetic Fe_3Si nanocrystals at the initial stages of crystallization.

3.2.3. Stage III: final stage of primary crystallization

In the second set of comparisons, the annealing temperatures for RA and CA were chosen to achieve the maximum crystalline volume fraction of $\sim$75–80 vol.% (determined from XRD in Fig. 5a–d) in the final stages of primary crystallization. Annealing at temperatures beyond those mentioned in Fig. 5a–d results in the onset of secondary crystallization, where the residual amorphous matrix crystallizes into Fe–B compounds, and that deteriorates the soft magnetic properties [5–13]. TEM investigation (not displayed here) also showed the nanostructure of the material after RA (both RA_1 and RA_2) and CA (both CA_1 and CA_2). Similar to the nanostructure obtained at the initial stage of primary crystallization (in Fig. 6a, c), individual Fe_3Si nanocrystals are separated by a thin layer ($<$1 nm) of amorphous matrix. The amorphous component is hardly detectable in the SAED pattern (not shown here), but it reveals the presence of nanocrystalline DO_3 structured Fe_3Si crystallites of significantly higher volume fractions. The grain sizes estimated from BF TEM images for both RA and CA with an average value of 10 ± 2 nm and 15 ± 3 nm, respectively, are in good agreement with the values measured from XRD (from Fig. 5a–d and in Fig. 2b). The crystallite sizes measured from TEM for all the four annealing conditions at the final stages of crystallization, including both RA and CA (images of which are not shown here), are summarized in Fig. 9a. Similar to the results obtained after initial stages of crystallization, RA has resulted in the formation of 30–50% smaller Fe_3Si nanocrystals at the final stages of primary crystallization.

The 3-D elemental maps of CA_1 (30 min at 575 °C), CA_2 (5 min at 655 °C), RA_1 (10 s at 555 °C) and RA_2 (4 s at 555 °C) specimens are shown in Fig. 8a–d. For better quantification and comparison with data obtained for the initial state of crystallization (in Fig. 7e–h), only Cu atoms with Cu clusters marked by isoconcentration surfaces are shown in Fig. 8e–h from a defined cylindrical sub-volume of $32 \times 32 \times 54$ nm^3 corresponding to Fig. 8a–d. In contrast to the initial stage of crystallization results, the average sizes of the Cu clusters are slightly larger for RA (including RA_1 and RA_2) than for CA (including CA_1 and CA_2), as can be seen in Fig. 9b. The proximity histograms corresponding to all the Cu clusters in Fig. 8a–d are shown in Fig. 8i–l. The Cu concentration in the core of the clusters were found to be ~100 at.% for all RA and CA conditions. Also, unlike the initial stage of crystallization, the number density of the Cu clusters obtained on RA and CA are almost identical, as summarized in Fig. 7d. The findings indicate that, with increasing annealing temperatures during both, RA and CA, the size of the Cu clusters has increased at the expense of a decreasing number density. This observation indicates the possibility of classical Ostwald ripening [33]. In contrast, higher number densities of Fe_3Si nanocrystals (~60–80%) are obtained at the final stages of crystallization on RA compared with CA (see Fig. 9c). This is a clear indication of nucleation dominating

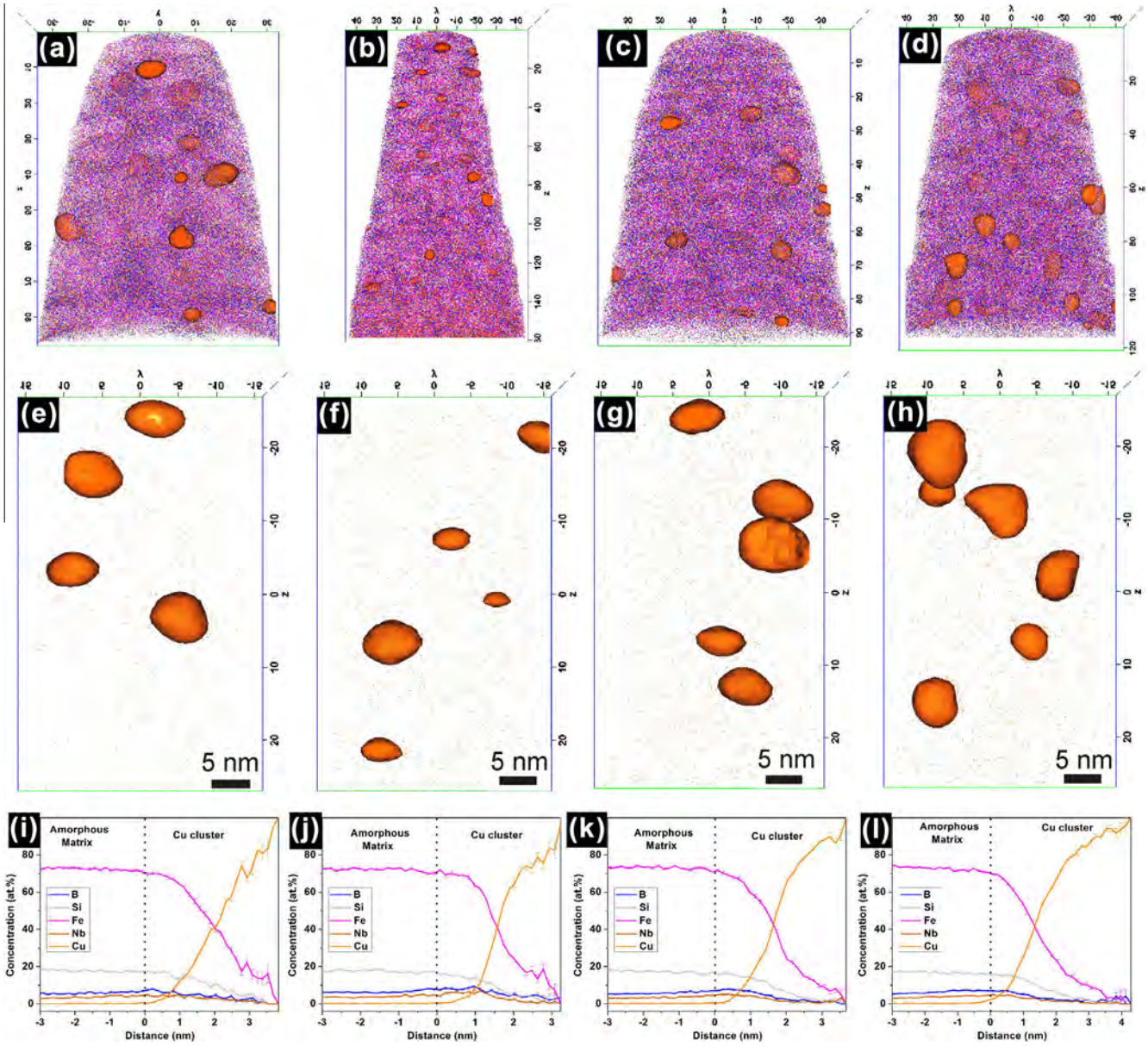

Fig. 8. APT elemental maps of Fe (●), Si (●), Nb (●), B (●), Cu (●) for: (a) CA_1, 575 °C 30 min; (b) CA_2, 655 °C 5 min; (c) RA_1, 695 °C 10 s; (d) RA_2, 695 °C 4 s. Cu atoms with isoconcentration surfaces (3 at.% Cu interface) showing Cu-rich clusters in a representative volume of $32 \times 32 \times 54$ nm^3 for: (e) CA_1, 575 °C 30 min; (f) CA_2, 655 °C 5 min; (g) RA_1, 695 °C 10 s; (h) RA_2, 695 °C 4 s. (i), (j), (k), (l) Proximity histogram of 0.15 nm bin size with respect to all the Cu clusters in the analysed volume of (a), (b), (c), (d) for CA and RA samples, respectively.

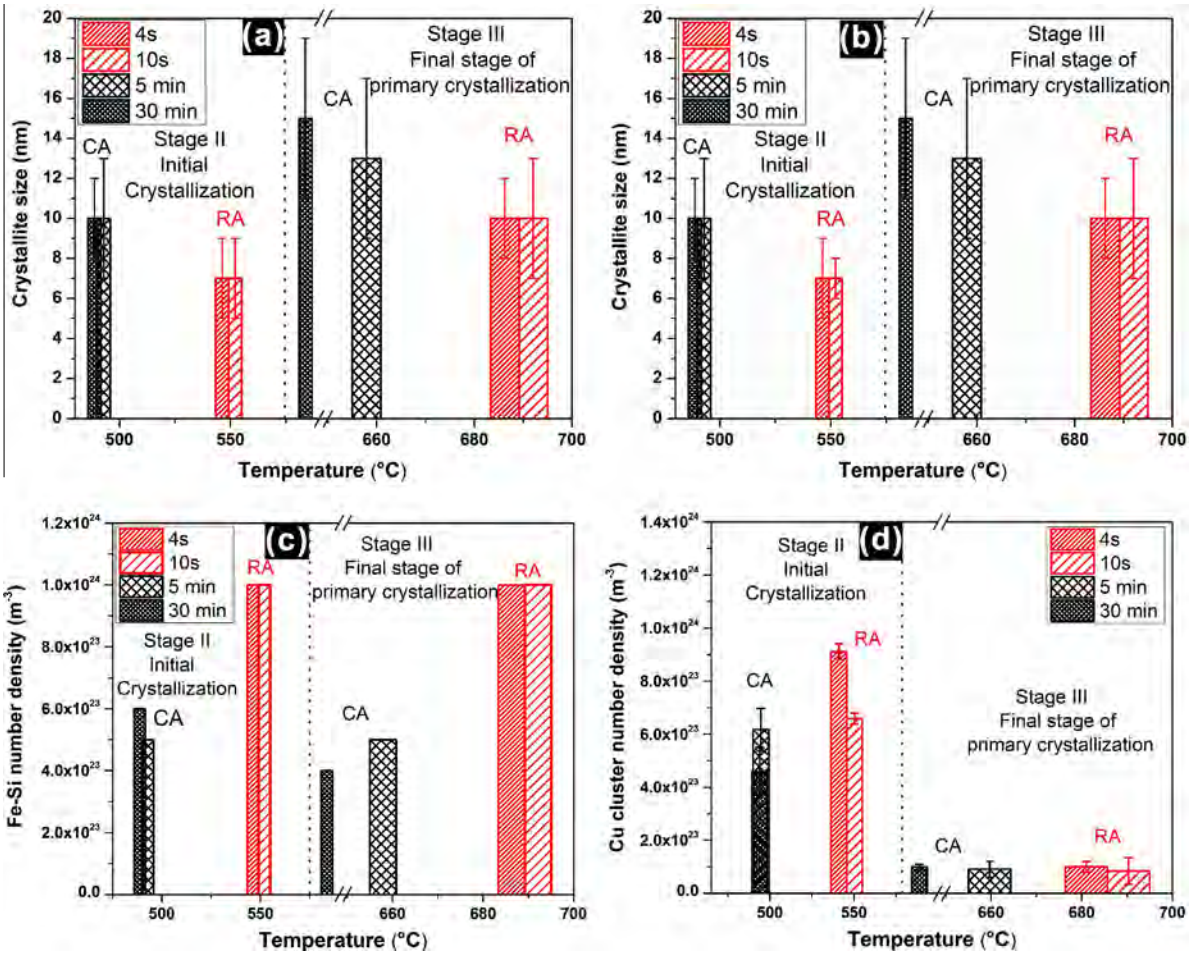

Fig. 9. Summary of (a) Fe_3Si nanocrystallite size, (b) Cu cluster size determined from APT, (c) calculated number densities of Fe_3Si nanocrystals N and (d) number density of Cu clusters estimated from the analysed volume of APT for RA and CA conditions: 4 s, RA_2; 10 s, RA_1; 5 min, CA_2; and 30 min, CA_1.

the growth process of Fe_3Si nanocrystals during RA. It can further be validated by the estimated 30% decrease in the number density of nanocrystals on CA_1, as shown in Fig. 9c, where longer annealing time seems to have facilitated growth. Therefore, it is suggested that nucleation is spontaneous during RA at higher temperatures, whereas growth is limited by the short annealing time, which results in progressive nucleation even at higher temperatures.

4. Discussion

4.1. Influence of Cu on Fe–Si nanocrystallization

4.1.1. Cu clusters as effective nucleation sites

The experimental results on RA clearly indicate that the onset of Cu clustering (~500 °C) occurs prior to the primary crystallization (~555 °C) of Fe_3Si nanocrystals. These observations are very similar and also in good agreement with the observations of Hono et al. [12], who showed that the Cu clusters are present in the amorphous matrix after annealing below the crystallization temperature under CA conditions. Therefore, the original purpose of having Cu clusters acting as heterogeneous nucleation sites seems to be satisfied on RA, but the effectiveness with which all the clustered Cu atoms act as potential heterogeneous nucleating sites for Fe_3Si nanocrystallization needs to be tested. SANS investigations on FINEMET and modified FINEMET alloys have particularly emphasized the need for having optimum Cu content in the alloy in order to achieve highest permeability [16]. The alloys optimized for Cu content show the highest number density of Cu clusters at the onset of primary crystallization, resulting in obtaining the finest possible Fe_3Si nanocrystalline structure at the final stages of crystallization, which determines the magnetic properties [16]. In contrast, the present observations clearly indicated a ~25% reduction in the number density of Cu clusters from the absolute maximum at the initial stages of crystallization (555 °C) (see Fig. 4). This indicates coarsening of Cu clusters prior to the primary crystallization event. To further validate this point, the onset of Cu clustering as ~500 °C for RA (as shown in Fig. 4) is now considered, based on the chosen cluster analysis parameters for filtering out realistic clusters, irrespective of the fact that the onset of Cu clustering was observed ~450 °C. The underestimated temperature difference between the onset of Cu clustering and primary

crystallization is >50 °C. Such a difference is large enough for coarsening to occur prior to the onset of crystallization [16]. Irrespective of this fact, a very high number density of Fe–Si nanocrystals in the order of $\sim 10^{24}\,m^{-3}$ was obtained, which is slightly higher than the actual number density of Cu clusters at the initial stages of crystallization during RA_2, but slightly lower in the case of RA_1 (see Fig. 9c and d). Even though the crystallographic information on the Cu clusters is unknown in the present work, these observations clearly indicate the effectiveness of Cu clusters serving as heterogeneous nucleation sites by inducing chemical inhomogeneities in the amorphous matrix, as shown by the proxigrams in Fig. 7i–l [15]. It can be concluded that a lower number density of nucleation sites than the maximum possible is, therefore, available during RA of an alloy with 1 at.% Cu, but the reduction in absolute values is still ~50% higher than that obtained on CA, as shown in Fig. 9d.

4.1.2. Coarsening mechanism

The experimental results indicate that the maximum Cu cluster number density is obtained after RA_2 at 535 °C, and coarsening of clusters starts prior to primary crystallization (555 °C), as can be noted from the decreasing number density with increasing annealing temperature (see Fig. 4). As indicated in Fig. 7g and h, there are instances where two Cu clusters are in direct contact with each other, the effect of which is also seen in the statistical proxigram in Fig. 7k and l, where the gradient in the Cu concentration fluctuates before reaching a maximum. These observations suggest that coarsening and coagulation of Cu clusters is activated in the amorphous matrix by bulk diffusion of Cu. To further understand the coarsening mechanism, a comparative view of the ambient Cu cluster environment between stage I and stage III specimens of the RA_2 condition is considered, as shown in Fig. 10. A cylindrical representative volume of $32 \times 32 \times 54\,nm^3$ with only Cu atoms and clusters in the form of isoconcentration surface corresponding to the 535 °C annealed condition from Fig. 3 is shown in Fig. 10a. Two Cu clusters interconnected by necks can be identified. A one-dimensional (1-D) concentration profile using a cylindrical volume of $1 \times 1 \times 15\,nm^3$ along the necking region (inset of Fig. 10b) of one of the interconnected cluster pairs marked by the rectangle in Fig. 10a is shown in Fig. 10b. Significant enrichment of Cu by a factor of at least 35 with respect to the Fe-rich amorphous matrix Cu concentration of 0.2 at.% is realized in the necking region. In contrast, during stage III coarsening, the Cu clusters are otherwise well separated from each other by the already nucleated Fe_3Si nanocrystals, as shown in Fig. 10c. Therefore, the environment necessary for early stage bulk Cu cluster coagulation as a coarsening mechanism is no longer possible. Thus, two different mechanisms are proposed for the concomitant Cu cluster growth and coarsening, namely: (a) a diffusion–coagulation mechanism of coarsening in the very early stages, namely, in stage I and to some extent at the beginning of stage II; and (b) classical Oswald ripening driven by the evaporation–condensation mechanism from the later part of stage II until the end of stage III.

The present investigation is a clear case where nucleation, growth and coarsening are occurring simultaneously as the Cu clusters evolve, which in an ideal case could be treated as distinct processes [33]. The primary reason behind the clustering of Cu atoms is the limited solubility of Cu in the α-Fe matrix [12,27]. As the clusters nucleate during annealing, the driving force for the reduction in interface energy initiates coarsening. The minimization of total energy when all the clusters coarsen into one huge Cu cluster mass is followed over a sequence of coarsening steps, as shown in Fig. 3 with respect to RA in the present case [33]. Therefore, the two different mechanisms proposed for Cu cluster coarsening are highly influenced by the surrounding environment. During stage I, Cu clusters nucleate vigorously and attain maximum densities before the primary crystallization, but are still present in a quasi-infinite amorphous matrix reservoir. Therefore, the average distances between two clusters are expected to be very small, so the probability of finding a nearest-neighbour Cu cluster with overlapping diffusion fields is high. As a result, during stage I and at the beginning of stage II with very low crystalline fraction, the suggested diffusion–coagulation mechanism can be activated [33,34]. Sudbrack et al. [34] made similar observations of precipitates following such a mechanism in a model Ni–Al–Cr superalloy. In contrast, in the later regime of stage II, when the crystalline fraction V_f reaches ~50% until the end of stage III, the Cu clusters are well separated from each other by the nucleated Fe_3Si nanocrystals, and so individual Cu atoms have to dissolve from smaller clusters and diffuse through the amorphous matrix to condense eventually at the larger clusters by the evaporation–condensation mechanism. From the experimental observations in Fig. 3, it is confirmed that the sequential coarsening of Cu clusters during RA_2 is governed by two different mechanisms, as mentioned above, and the relevance of either of them being active depends on the ambient surrounding environment.

4.2. Mechanism of Fe–Si nanocrystallization

As shown in Fig. 9c, an estimated 60–80% increase in the number density of Fe_3Si nanocrystals is obtained on RA in the initial stages of crystallization, i.e. stage II. The above estimation correlates well with the identical increase in the number density of Cu clusters on RA compared with CA, as shown in Fig. 9d. Therefore, a direct one-to-one relationship exists between the number densities of clustered Cu atoms and the nucleated nanocrystals for both RA and CA, which is also in good agreement with the observations of Hono et al. [12]. However, during the final stages of crystallization in stage III, the number densities of Cu cluster decreased to a minimum, and yet there was no observable reduction in the number density of the nanocrystals. Therefore, it could be inferred that there is

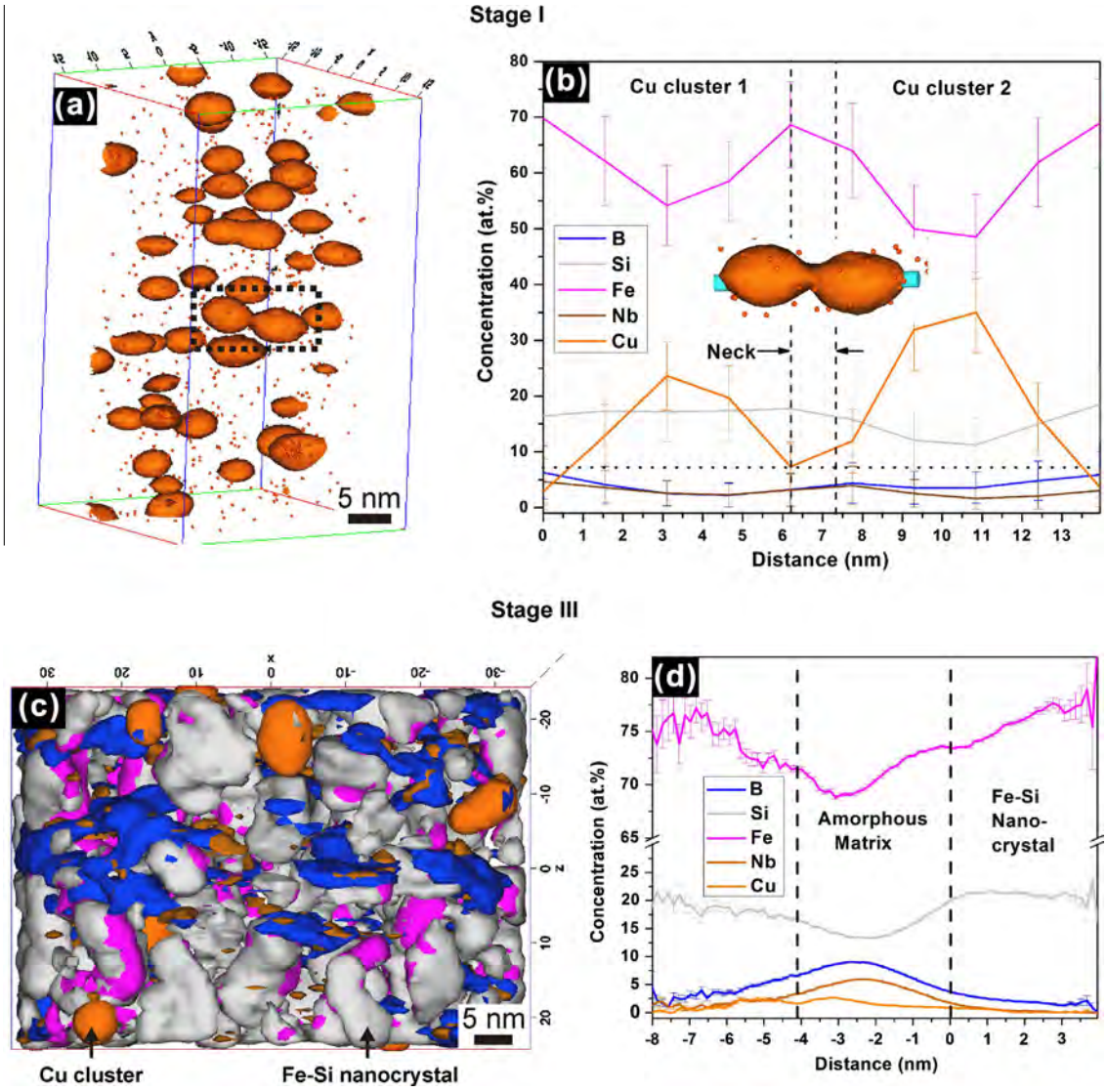

Fig. 10. (a) APT elemental maps of Cu (●) and Cu-rich clusters delineated by 3 at.% isoconcentration surfaces in a representative volume of $32 \times 32 \times 54$ nm^3 for stage I, RA_2: 535 °C 4 s. (b) 1-D concentration profile along a cylindrical volume of $1 \times 1 \times 15$ nm^3 along the necking region (shown in inset) of one of the interconnected cluster pair marked by rectangle in (a). (c) 3-D elemental map of RA_2: 695 °C 4 s, stage III final crystallization with all the alloying elements in their respective isoconcentration surfaces clearly depicting the actual nanostructure of the alloy. Isoconcentration values Fe: 80 at.% (●), Si 20 at.% (●), Nb 8 at.% (●), B 13 at.% (●), Cu 3 at.% (●). (d) Proximity histogram of 0.15 nm bin width with respect to all the Si-rich regions in (c), indicating the composition of the Fe–Si nanocrystals and the amorphous matrix.

progressive nucleation in spite of decreasing heterogeneous nucleation sites. In the present work, the structure of the Cu clusters was not determined, but it has already been established with considerable evidence from X-ray absorption fine structure measurements that the Cu clusters attain a nearest-neighbour structure similar to face-centred cubic (fcc) Cu directly from the amorphous matrix [31,35,36]. Based on such observations, Hono et al. [12] proposed the heterogeneous nucleation model for Fe–Si nanocrystallization on the surface of fcc Cu clusters, following the rationale that the interfacial energy is minimum following either the Nishiyama–Wasserman or the Kurdjumov–Sachs orientation relationship, supported chemically by the pile-up of Fe atoms around the clusters. Alternatively, there were also reports on the possibility of chemical fluctuation induced Fe–Si nanocrystallization as Cu atoms substitute Fe atoms during clustering, resulting in regions of Fe or Si enrichment, which also crystallize separately from Cu-rich regions [15]. In addition, Chen et al. [14] demonstrated that only those Cu clusters that are in the size range of 4–5 nm act as heterogeneous nucleation sites. Thus, several reports have shown experimentally the various possible modes of nanocrystallization. In the present investigation, particularly during RA, the overall duration for processing is only a few seconds (4–10 s), irrespective of the annealing temperatures used. Therefore, the mechanism of Fe–Si nanocrystallization could be a combination of chemical fluctuation induced Fe–Si enrichments in the

amorphous matrix, which might then crystallize homogeneously because of the higher annealing temperatures achieved during RA, irrespective of the structural influence exerted by supposedly crystalline Cu clusters.

In order to understand the Fe–Si nucleation mechanism better, the diffusivity of Fe was estimated. Owing to the fact that Fe is the major matrix element and subsequent diffusion of Si into Fe-rich regions followed by DO_3 ordering is only a second order transition, Si diffusivity has a limited effect on the nucleation process [12]. Also, the XRD peak in Fig. 2a close to the onset of crystallization does not show any additional peaks corresponding to DO_3 ordering, but these are visible at later stages. Assuming that the diffusivity of Fe D_{Fe} is independent of concentration and assuming further spherical crystals of radius r, D_{Fe} can be estimated using the equation

$$r = \alpha\sqrt{D_{Fe}t} \tag{2}$$

where t is the annealing time, and α a dimensionless parameter evaluated from the concentration at the crystal–amorphous matrix interface [37,38]. The present analysis gives minimum Fe diffusivities of 1.3×10^{-17} m^2 s^{-1} and 2.5×10^{-17} m^2 s^{-1} for RA_2 at the onset of crystallization (555 °C) and at the final stages of crystallization (695 °C), respectively. The estimated values for RA are orders of magnitude higher than the estimated diffusivities during CA ($\sim 10^{-20}$ m^2 s^{-1}), which are in good agreement with the bulk diffusivities in Finemet alloys at 490 °C, where Nb diffusion in the amorphous matrix was found to be growth controlling [38]. Such an increase is expected, as RA proceeds at higher temperatures than CA by at least 100 °C. This finding implies that RA leads to higher diffusion lengths of Fe (thermally driven) than CA. Thus, the crystallization of clustering-induced Fe–Si-enriched regions in the amorphous matrix is highly likely, considering the temperature effect in addition, to a limited extent, to the direct Cu cluster-induced heterogeneous nanocrystallization.

4.3. Heterogeneous nucleation model

Hono et al. [12] proposed a heterogeneous nucleation model based on their observation of Cu clusters at the interface of the Fe-rich nanocrystals and the rest of the amorphous matrix using APT. This model was slightly different from the earlier proposed model of Ayers et al. [31], where the nanocrystals were shown to be enveloping the Cu clusters during growth. The present results further confirm that the Cu clusters form in the amorphous matrix and coarsen prior to nanocrystallization, as shown in Fig. 10a. After the final stages of crystallization (see Fig. 10c), a certain number of clusters are found to be in direct contact with Fe–Si nanocrystals, but at the nanocrystal/amorphous matrix interface. This observation confirms that the nanocrystals do not envelope Cu clusters during growth, i.e. the model proposed by Hono et al. [12] applies. However, there are some differences in the mode of crystallization, which are described below in detail.

Based on the experimental results and observations at three different stages of RA, a modified heterogeneous nucleation model is proposed for RA, as shown by a schematic in Fig. 11. In the as-prepared amorphous condition, all the elements are randomly distributed. On annealing prior to the onset of primary crystallization, i.e. stage I, Cu atoms form clusters by rejecting all the other atoms. At this stage, the measured Cu concentration in the clusters, as shown in Fig. 10b, is ~25 at.%, with an average size of ~1.5 nm diameter (see Fig. 4). As per the earlier reports, Cu concentration as low as ~25 at.% measured at this stage is unlikely to have a close-packed fcc structure as well as a size is small enough to play an active role in Fe–Si nanocrystallization [14,36]. But a certain fluctuation in the distribution of other elements (see Fig. 10b), including localized enrichments of Fe and Si atoms at random sites marked by a dotted rectangle (expected to be ⩽1 nm in size) are created in the amorphous matrix, owing to the clustering of Cu atoms. Such enrichment is highly likely to transform into a nanocrystal at slightly higher temperatures, irrespective of the structure of the Cu cluster. Moreover, it is shown in Figs. 4 and 10a that the coarsening of Cu clusters is also observed at this stage, and so the number of nucleation sites will be decreased during the onset of primary crystallization. Following the same argument, it is obvious that the higher the number density of Cu clusters prior to crystallization, the higher the availability of Fe

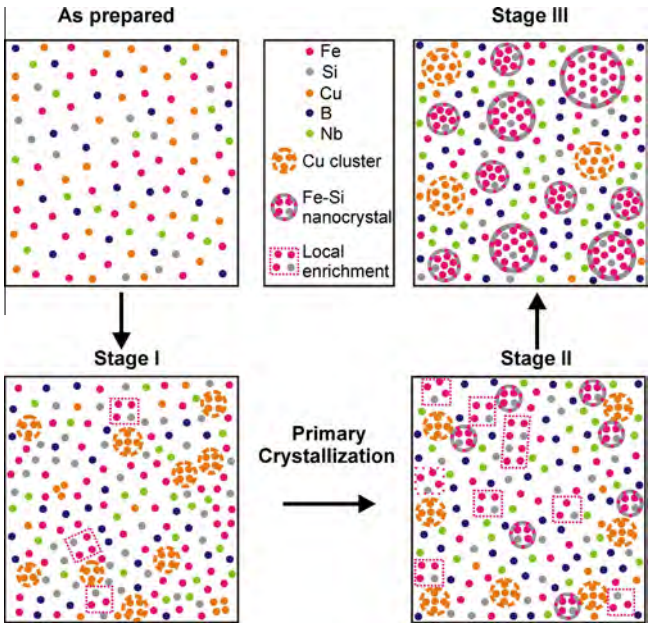

Fig. 11. Schematic illustration of the nanostructure evolution during RA of amorphous $Fe_{73.5}Si_{15.5}Cu_1Nb_3B_7$ alloy by primary crystallization. The chemical fluctuation caused by the Cu clusters can induce Fe–Si nanocrystallization as Cu atoms substitute Fe atoms during clustering, resulting in regions of Fe or Si enrichment, so that individual Fe–Si nanocrystallization independent of Cu clusters becomes possible [15].

enrichment. The observed cluster–coagulation mechanism of Cu cluster growth at this stage will increase the formation of Fe-rich regions.

During stage II of RA, the Cu clusters l have already coarsened to ~2.5 nm in size (see Fig. 4), and the onset of primary crystallization is realized. Also, the Cu concentration of clusters is increased significantly at this stage to >95 at.% (see Fig. 7k and l). The Cu clusters can have a similar structure to that of fcc Cu only beyond this stage. As depicted in Fig. 11, the progressive coarsening will result only in increasing the number density of Fe enriched regions, while crystallizing the already enriched regions into Fe-rich nanocrystals. Until now, the role of Cu clusters as a heterogeneous nucleation site can only be considered in terms of structures inducing chemical fluctuations, while in stage III, the Cu clusters should be fully crystallized, considering their significantly coarsened size (5–6 nm from Fig. 4). However, according to previous reports, only these Cu clusters can nucleate Fe–Si nanocrystals based on structural orientation relationships, as discussed earlier [14]. In contrast, at stage III, a minimum Fe–Si crystalline fraction of ~60 vol.% has already formed, which strongly supports the suggestion that the chemical fluctuations induced by Cu clustering are actually responsible for the Fe–Si nanocrystallization. This effect is referred to as a pseudo-homogeneous nucleation mechanism, since the nucleation proceeds homogeneously, but it does so inside a matrix that is chemically inhomogeneous owing to the preceding chemical matrix decomposition caused by the Cu clustering. Such an argument is further strengthened by Fig. 9c and d, where the number density of Cu clusters has decreased to a minimum at stage III, but the Fe–Si nanocrystal number density remains high, of order $\sim 10^{24}\ m^{-3}$, similar to the estimated values at the initial stages of crystallization (stage II). Considering the extremely short time (4–10 s) of processing during RA, it is highly unlikely that every Fe–Si nanocrystal nucleates along the periphery of Cu clusters and diffuses into the amorphous matrix as a bulk nanocrystal.

A confirmation of the effect proposed here can be realized from the stage III experimental result shown in Fig. 10c. The 3-D elemental map of the 695 °C 4 s annealed sample showing Cu clusters, Fe–Si nanocrystals and the amorphous matrix in terms of their respective isoconcentration surfaces depicts the nanostructure in a more realistic topological fashion. It must be noted that the different stages studied during RA are concomitant. From Fig. 10c, it is obvious that only a few Fe–Si nanocrystals are found to be in close proximity to the Cu clusters, while a majority of nanocrystals are well separated from the Cu clusters. This topological observation further confirms the proposed model of chemical fluctuation-induced nanocrystallization. Spontaneous nanocrystallization from a fully amorphous state during RA indicates that the higher crystallization temperatures achieved as a result of higher heating rates enforce crystallization of locally enriched regions. Similar behaviour of spontaneous crystallization has been noticed on Finemet alloys during DC Joule heating, where high heating rates comparable with RA were achieved [17,39]. The measured Si concentration in the nanocrystals during stage III (~21 at.% from Fig. 10d) is higher compared with those measured during stage II (~18 at.% from Fig. 7i–l). Therefore, RA produces chemically and structurally similar types of nanocrystals compared with that of CA, which is also in good agreement with previous reports [11,12,27]. Therefore, the mechanism of chemical fluctuation induced nanocrystallization proposed here is similar to earlier suggestions except for the fact that massive nucleation of Fe–Si nanocrystals occurs pseudo-homogeneously during RA [12].

4.4. Magnetic properties

The smaller grain size achieved in these alloys reduces the average contribution of the magneto-crystalline anisotropy associated with the randomly oriented grains, and so provides potential for yielding improved soft magnetic properties [40]. However, for the present alloy composition, the grain size after CA is already so small (~15 nm) that the random anisotropy contribution is hardly visible, such that the soft magnetic properties are rather determined by more macroscopic anisotropy contributions (magneto-elastic or annealing-induced anisotropy) and/or the surface quality of the ribbons [40,41]. The RA_2 samples revealed a small creep-induced anisotropy of $\sim 500\ J\ m^{-3}$, since a minimum stress is necessary to continuously transport the ribbons through the furnace [13]. This anisotropy is about two orders of magnitude larger than the random anisotropy contribution and governs the magnetization process [13,41]. Therefore, within the experimental scatter, the coercivity is about the same as in the case of CA under the same stress conditions.

5. Summary and conclusions

The nanostructure of a $Fe_{73.5}Si_{15.5}Cu_1Nb_3B_7$ alloy at three different stages of nucleation and growth cycle on RA and CA was investigated using XRD, TEM and APT. The following conclusions are drawn.

1. In spite of employing a set of extremely different annealing conditions, the final Fe–Si nanocrystalline structure and the chemical composition remain basically the same.
2. APT revealed the simultaneous onset and coarsening of Cu clusters during stage I, i.e. prior to primary crystallization on RA. These clusters act as indirect heterogeneous nucleation sites by inducing chemical inhomogeneities in the amorphous matrix. These chemical heterogeneities in the amorphous matrix act as nuclei during nanocrystallization. This mechanism is referred to as chemical fluctuation-induced nanocrystallization.

3. RA resulted in the formation of ~30% smaller Fe–Si nanocrystals with very high number densities of the order of $\sim 10^{24}$ m^{-3} compared with CA during the final stages of crystallization. This is a direct consequence of a shorter processing time (4–10 s) during RA at higher annealing temperatures, where growth is restricted. Therefore, a nucleation-dominated mechanism of nanocrystallization is introduced.
4. The coarsening of Cu clusters starts initially by a diffusion–coagulation mechanism in the amorphous matrix prior to primary crystallization. On sufficient (>50 vol.%) crystallization, the coarsening is further driven by classical Ostwald ripening through the conventional evaporation–condensation mechanism.
5. The observed coarsening of Cu clusters prior to primary crystallization during RA has resulted in a reduction in the number density of available nucleation sites, which opens up the possibility for further optimization of the Cu content, enabling new alloy design opportunities.
6. Even though the coarsening of Cu clusters was observed during the initial stages of crystallization, RA still yields a ~80% higher number density of Cu clusters compared with CA.

Acknowledgement

The authors would like to thank Dr. Masato Ohnuma (Hokkaido University, Japan) for helpful discussions.

References

[1] Yoshizawa Y, Oguma S, Yamauchi K. J Appl Phys 1988;64:6044.
[2] Yoshizawa Y, Yamauchi K. Mater Trans JIM 1990;31:307.
[3] Yoshizawa Y, Yamauchi K. IEEE Trans Magn 1989;25:3324.
[4] Yoshizawa Y, Fujii S, Ping DH, Ohnuma M, Hono K. Scripta Mater 2003;48:863.
[5] Herzer G. Mater Sci Eng A 1991;133:1.
[6] Herzer G. Acta Mater 2013;61:718.
[7] Herzer G, Flohrer S, Polak Ch. IEEE Trans Magn 2010;46:341.
[8] Herzer G. Soft magnetic materials – nanocrystalline alloys. In: Kronmüller Helmut, Parkin Stuart, editors. Handbook of magnetism and advanced materials. Novel materials. New York: John Wiley, vol. 4; 2007. p. 1882.
[9] Flohrer S, Schäfer R, Herzer G. J Non-Crystal Sol 2008;354:5097.
[10] Hono K, Inoue A, Sakurai T. Appl Phys Lett 1991;58:2180.
[11] Herzer G. Nanocrystalline soft magnetic alloys. In: Buschow KHJ, editor. Handbook of magnetic materials, vol. 10. Amsterdam: Elsevier; 1997.
[12] Hono K, Ping DH, Ohnuma M, Onodera H. Acta Mater 1999;47:997.
[13] Herzer G, Budinsky V, Polak C. Phys Status Solidi B 2011;248:2382.
[14] Chen YM, Ohkubo T, Ohta M, Yoshizawa Y, Hono K. Acta Mater 2009;57:4463.
[15] Hono K, Li JL, Ueki Y, Inoue A, Sakurai T. Appl Surf Sci 1993;67:398.
[16] Ohnuma M, Hono K, Linderoth S, Pedersen JS, Yoshizawa Y, Onodera H. Acta Mater 2000;48:4783.
[17] Allia P, Baricco M, Knobel M, Tiberto P, Vinai F. J Mag Mag Mater 1994;133:243.
[18] Cullity BD, Stock SR. Elements of X-Ray diffraction. Upper Saddle River, NJ: Prentice Hall; 2001.
[19] Pradeep KG, Wanderka N, Choi P, Banhart J, Murty BS, Raabe D. Acta Mater 2013;61:4696.
[20] Miller MK, Cerezo A, Hetherington MG, Smith GDW. Atom probe field ion microscopy. Oxford: Clarendon Press; 1996.
[21] Miller MK. Atom probe tomography analysis at the atomic scale. New York: Kluwer Academic/Plenum; 2000.
[22] Kelly TF, Miller MK. Rev Sci Instrum 2007;78:031101.
[23] Seidman D. Annu Rev Mater Sci 2007;37:127.
[24] Marquis EA, Miller MK, Blavette D, Ringer SP, Sudbrack CK, Smith GDW. MRS Bull 2009;34:725.
[25] Isheim D, Gagliano MS, Fine ME, Seidman DN. Acta Mater 2006;54:841.
[26] Raabe D, Choi P, Li Y, Kostka A, Sauvage X, Lecouturier F, et al. MRS Bull 2010;35:982.
[27] Hono K. Prog. Mater. Sci. 2002;47:621.
[28] Thompson K, Lawrence D, Larson DJ, Olson JD, Kelly TF, Gorman B. Ultramicrosc 2007;107:131.
[29] Marquis EA, Hyde JM. Mater Sci Eng R 2010;69:37.
[30] Vurpillot F, Bostel A, Blavette D. Appl Phys Lett 2000;76:3127.
[31] Ayers JG, Harris VG, Sprague JA, Elam WT, Jones HN. Acta Mater 1998;46:1861.
[32] Mattern N, Danzig A, Müller M. Mater Sci Eng A 1995;194:77.
[33] Wagner R, Kampmann R, Voorhees PW. Homogeneous second-phase precipitation. In: Kosortz G, editor. Phase transformations in materials. Weinheim: Wiley-VCH; 2001. p. p. 309.
[34] Sudbrack CK, Yoon KE, Noebe RD, Seidman DN. Acta Mater 2006;54:3199.
[35] Sakurai M, Matsuura M, Kim SH, Yoshizawa Y, Yamauchi K, Suzuki K. Mater Sci Eng A 1994;A179/A180:469.
[36] Kim SH, Matsuura M, Sakurai M, Suzuki K. Jpn J Appl Phys 1992;32:676.
[37] Köster U. Key Eng Mater 1993;81–83:647.
[38] Köster U, Schünemann U, Blank-Bewersdorff M, Brauer S, Sutton M, Stephenson GB. Mater Sci Eng A 1991;133:611.
[39] Allia P, Baricco M, Tiberto P, Vinai F. Rev Sci Instrum 1993;64:1053.
[40] Herzer G. IEEE Trans Magn 1990;26:1397.
[41] Herzer G. J Magn Magn Mater 2005;294:99.